Dynamics of a non-linearly damped microresonator under parametric excitation and its application in developing sensitive inertial sensors with ultra-wide dynamic ranges

S. Amir Mousavi Lajimi

University of Waterloo and Infigo Tronix Ltd., Canada

Michael I. Friswell

College of Engineering, Swansea University, Swansea SA1 8EN, UK

Abstract

We model and investigate the response of a nonlinear cantilever beam under principal parametric excitation. The design is initially assessed, optimized, and tuned using three-dimensional finite element analysis (FEA) to ensure the presence of fundamental parametric resonance and the absence of other internal and higher-order parametric resonances. The derived governing differential equation represents a modified generalized parametrically excited dynamic system under principal parametric excitation. The nonlinear dynamic system is developed and presented in the context of resonators with extensive applications in developing sensors, filters, and switches. The quadratic and cubic nonlinearities include second- and third-order deflection, velocity, acceleration terms describing stiffness, inertial, and damping nonlinearities. To explore and investigate the corresponding generalized nonlinear Mathieu equation, the method of multiple-scales along with the reconstitution method are used and modulation equations are obtained and solved to obtain closed-form amplitude and phase equations. The quadratic damping is modeled and approximated using a Fourier series and analytical models are generated in both Cartesian and Polar frames. To fur-

Email addresses: amir.lajimi@uwaterloo.ca, samousav@uwaterloo.ca (S. Amir Mousavi Lajimi), m.i.friswell@swansea.ac.uk (Michael I. Friswell)

ther explore the dynamic system and its applications, a resonator is designed to measure external acceleration and investigated for two cases. It is discussed and shown how the external acceleration modifies the dynamic system, the corresponding reduced-order model, and the modulation equations. The external acceleration affects the amplitude, phase, and frequency of oscillation providing means to estimate the input. These results indicate that the proposed resonator design (dynamic system) is able to significantly improve the dynamic range of shock/acceleration sensors.

Keywords: Generalized parametric resonance, nonlinear dynamics, quadratic damping, inertial and stiffness nonlinearity, bifurcation, sensors, FEA

---

1. Introduction

Varying the parameters of a system periodically, either stiffness or mass, may result in stable or unstable system responses. Mathieu [1] and Hill [2] were the pioneers who studied the phenomena and developed equations of motion for parametrically excited dynamical systems. The amplitude and frequency of the parameter variation at which the trivial equilibrium becomes unstable depends on the ratio of the frequency to the natural frequency of the system and the energy dissipation during a cycle. Parametric resonance appears in various areas of applied mechanics from surface wave propagation to the micro and nano-electromechical systems (M/NEMS). The principal parametric resonance (PR) occurs when the parameter varies two times faster than the natural frequency of the system *i.e.* $\hat{\omega}/\hat{\omega}_n \approx 2$. Higher order PR occurs for $\hat{\omega}/\hat{\omega}_n \approx 2/n$ where n is a positive integer. Recently, various experimental studies have shown the possibility of generating higher-order PR windows [3, 4, 5].

Given the wide range of applications and the importance of PR an extensive literature has investigated the underlying mathematical physics of parametrically excited dynamical systems. Zavodney and Nayfeh [6] studied macro uniform cantilevers under principal parametric excitation (PPE) and concluded that PPE results in large amplitude vibration and specimen failure under low

damping. They observed hardening behaviour under PPE and some discrepancies between the numerical and experimental results. Balachandran and Nayfeh [7] and Nayfeh and Balachandran [8], further studied the effect of quadratic nonlinearities under various resonance conditions using perturbation analysis. Anderson et al. [9] introduced quadratic damping into the mathematical model and observed a better agreement between the single-mode perturbation method and experimental results. Both studies showed the strength of the curvature nonlinearity in the absence of any softening-type term in the equation of motion. Revisiting the mathematical model of Zavodney and Nayfeh, Meesala and Hajj [10] studied the effect of statically varying mass and stiffness parameters on the type of bifurcation and the number of limit cycles.

Ng and Rand studied a Mathieu equation with cubic nonlinearity using analytical and continuation methods and provided a comprehensive picture of bifurcation diagrams for principal PR [11]. Variations of the Mathieu-Hill equation (MHE), such as the forced MHE, have also been investigated. Li et al. [12] studied a periodically forced MHE and verified the accuracy of using the method of variation of parameters for the response analysis. PR can also be generated and achieved through feedback loops [13, 14]. In both cases, a reduced-order single mode model including quadratic damping was able to capture the dynamics of the system.

Employing parametric excitation (PE) to develop novel resonators, sensors, and energy harvesters is becoming increasingly common [15, 16, 17, 18, 19, 20]. Belhaq et al. [21] studied a time-delayed modified MHE and provided some results concerning the performance of such systems in relation to their application in developing energy harvesting mechanisms. PR may also be activated through modulating the intensity of an emitting light on a graphene membrane and the consequent change in internal strain [22]. Modeling the membrane response with a modified Matthieu equation shows good agreement with the experimental results at low level excitation. In nanomechanics, nonlocal nanobeams under PE qualitatively show similar stability behaviour as local beams [23] with a more pronounced size effect. Potential applications of PR in atomic force microscopy

(AFM) and scanning probe microscopy (SPM) are discussed by Moreno-Moreno et al. [13] and Prakash et al. [14].

There has been significant effort to develop energy harvesters benefiting from PR, and especially PPR. The advantage of PE over direct excitation to develop vibration energy harvesters is particularly evident in weakly nonlinear systems where a larger bandwidth is generated using PE [24]. Using a perturbation approach Daqaq et al. [25] analyzed a cantilever beam under base excitation and presented parametric resonance as a viable option for energy harvesting. Auto-parametric resonance, as well as parametric resonance, demonstrates promising potential for energy harvesting in real applications [26]. Although parametric resonance, in contrast to direct resonance, is not limited by linear damping, its onset or activation is negatively affected by increasing linear damping [27]. There has also been some effort devoted to employing PR in developing inertial sensors, particularly gyroscopes [28, 29, 17]. In the following we mostly focus on developing a resonator to design a large-range accelerometer.

In this work, we develop a modified dynamic system including electrostatic force and external acceleration for generalized parametric resonance. A T-shape structure under PPE is considered and the corresponding single-mode Mathieu equation is developed. A quadratic as well as linear dissipating term is included in the equation of motion. Electrostatic, geometric and inertial nonlinearities are included in our analysis. A Heaviside function is used to properly describe the electrostatic moving side load. Once the single-mode Mathieu equation is obtained, the method of multiple scales is used to compute and study the slow dynamics of the system. To further show an application of the analysis an acceleration/shock/impact sensor is developed and studied based on analytical and numerical results. It is shown that the proposed dynamic system can be used to fabricate a robust design for an extremely wide dynamic range acceleration sensor.

The ultimate goal is to develop a shock/impact/motion/acceleration sensor with an extremely wide (and adjustable) dynamic full-scale range. The objective is the ability to adjust the dynamic range of acceleration up to several

hundred thousand g, where g is the gravitational acceleration. The system may be used to actuate another system or to generate a signal. The output of the resonator is characterized and calibrated versus the (unknown) input acceleration to detect and characterize the external shock/impact/momentum/motion. Depending on the (unknown) input acceleration, the use of an amplitude-based or a frequency-based measurement method is proposed. This allows very small responses, even at the molecular level, to be directly transduced into a micromechanical response, which can be measured by the cantilever deflection and/or its resonance-frequency shift.

2. Mathematical modeling: deriving the equation of motion

The ultimate goal is to generate parametric resonance, and therefore the resonator may have any shape, in principle. However, from the authors' past experience, a cantilever placed on a base structure is a reliable yet simple choice. At the micro scale the difficulty of the fabrication process would increase, requiring more complex designs. Even including a large end-mass would increase the probability of stiction, a common cause of failure in micro devices. In principle, any design accommodating a principal parametric resonance can be used. For example, Nitzan et al. (among others) discuss a disk gyroscope under self-induced parametric resonance [30] and Lajimi et al. proposed the use of an H-shaped structure to exploit parametric resonance [17]. However, these designs are complicated in comparison to a simple cantilever-based design. Hence, the T-shape oscillator shown in Fig. 1 is considered and the corresponding enhanced Mathieu-Hill equation is derived. The structure includes a base (primary) resonator, a secondary (cantilever) resonator, and a pair of electrodes to detect the induced motion. The frequency-tuning electrodes are placed far enough from the tip of the cantilever resonator to keep the forcing area and the average bias load constant as the resonator oscillates. The base (primary) resonator is used to pump energy into the secondary resonator and excite its principal parametric resonance, creating an auto-parametrically excited dynamic system.

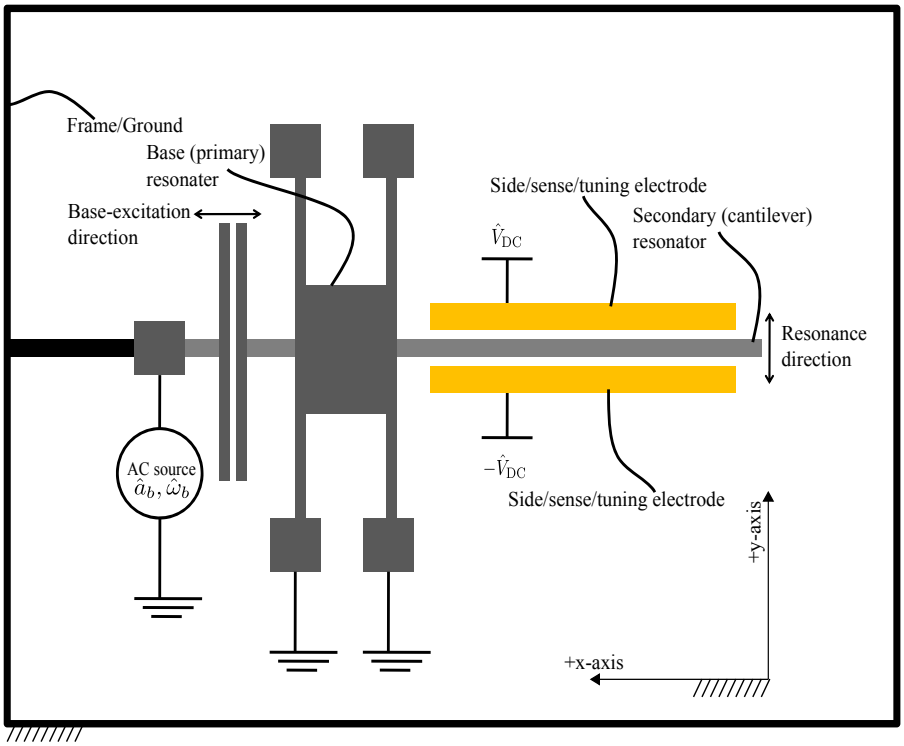

Figure 1: A cantilever beam under parametric base-excitation.

Considering Crespo da Silva and Glynn's [31] mathematical model and following [32], the axial force is described by

$$\hat{p}(\hat{s},\hat{t}) = -\hat{m}(\hat{l}-\hat{s})\hat{a}_b\,\hat{\omega}_b^2\,\cos(\hat{\omega}_b\,\hat{t}) \tag{1}$$

and is substituted into $\dfrac{\partial}{\partial \hat{s}}\left[\hat{p}(\hat{s},\hat{t})\dfrac{\partial \hat{v}(\hat{s},\hat{t})}{\partial \hat{s}}\right]$ to generate the following term in the equation of motion

$$\hat{m}\left[(\hat{s}-\hat{l})\hat{v}'' + \hat{v}'\right]\,\hat{a}_b\,\hat{\omega}_b^2\,\cos(\hat{\omega}_b\,\hat{t}) \tag{2}$$

where $\hat{a}_b\,\hat{\omega}_b^2\,\cos(\hat{\omega}_b)$ indicates the dynamic applied acceleration. The linear mass density is represented by $\hat{m}$, the amplitude of base-excitation by $\hat{a}_b$, the frequency of base excitation by $\hat{\omega}_b$, the beam (resonator) length by $\hat{l}$, the length variable along the length of the resonator by $\hat{s}$, and the transverse of resonance

by $\hat{v}$ (dropping the length and time variables for clarity of notation, that is $\hat{v} \equiv \hat{v}(\hat{s},\hat{t})$).

The fringing field affects the parallel-plate capacitor and therefore is included in the force-model by implementing a first-order correction factor [33]. Thus, adding together the force vectors for both electrodes, the transverse electrostatic force (per unit length) is:

$$\hat{f}_{es}(\hat{s},\hat{t}) = \frac{1}{2}\,\hat{\epsilon}\,\hat{h}_e\,\frac{\hat{l}_e}{\hat{l}}\,\hat{V}(\hat{t})^2\left(\frac{1+0.65\frac{(\hat{d}-\hat{v}(\hat{s},\hat{t}))}{\hat{h}_e}}{\left(\hat{d}-\hat{v}(\hat{s},\hat{t})\right)^2}-\frac{1+0.65\frac{(\hat{d}+\hat{v}(\hat{s},\hat{t}))}{\hat{h}_e}}{\left(\hat{d}+\hat{v}(\hat{s},\hat{t})\right)^2}\right)$$
$$\times(H(\hat{s}-(\hat{l}_b+\hat{f}_b(\hat{t})))-H(\hat{s}-(\hat{l}_e+\hat{l}_b+\hat{f}_b(\hat{t})))) \qquad (3)$$

where $\hat{l}_e$ is the length of side electrodes, $\hat{l}_b$ is the distance from the electrode to the base, $\hat{d}$ is the gap between the side electrodes and the resonator, $\hat{h}_e$ is the width of the electrodes (perpendicular to the resonance direction), and $\hat{\epsilon}$ is the permittivity. $\hat{V}(\hat{t})$ is the supplied voltage to the side electrodes; in this paper a DC bias-voltage will be assumed, i.e. $\hat{V}(\hat{t}) = \hat{V}_{\mathrm{DC}}$. H denotes the Heaviside function that gives a nonzero electrostatic force only when the electrodes are present. The positions of the ends of the electrodes are given by $\hat{s}_1(\hat{t}) = \hat{l}_b + \hat{f}_b(\hat{t})$ and $\hat{s}_2(\hat{t}) = \hat{l}_e + \hat{l}_b + \hat{f}_b(\hat{t})$. Therefore, for a nonlinear beam with an axial force, base-excitation, and including linear and quadratic damping, the equation of motion is [34]:

$$\hat{E}\,\hat{I}\,\hat{v}'''' + \hat{m}\,\ddot{\hat{v}} + \hat{\alpha}\,\dot{\hat{v}} = \hat{F}_{\mathrm{qd}} + \hat{F}_{\mathrm{ns}} + \hat{F}_{\mathrm{ni}} + \hat{F}_{\mathrm{be}} + \hat{F}_{es} \qquad (4)$$

$$\hat{F}_{\mathrm{qd}} = -\hat{\beta}\,\dot{\hat{v}}|\dot{\hat{v}}|$$
$$\hat{F}_{\mathrm{ns}} = -\hat{E}\,\hat{I}\left(\hat{v}'^2\hat{v}''' + \hat{v}'\hat{v}''^2\right)'$$
$$\hat{F}_{\mathrm{ni}} = -\frac{1}{2}\hat{m}\left[\hat{v}'\int_{\hat{l}}^{\hat{s}}\left[\frac{\partial^2}{\partial\hat{t}^2}\int_0^{\hat{s}}\hat{v}'^2\,\mathrm{d}\hat{s}\right]\mathrm{d}\hat{s}\right]'$$
$$\hat{F}_{\mathrm{be}} = -\left[\hat{m}(\hat{s}-\hat{l})\hat{v}'' + \hat{m}\hat{v}'\right]\,\hat{a}_b\,\hat{\omega}_b^2\,\cos(\hat{\omega}_b\,\hat{t})$$

$$\hat{F}_{es} = \frac{1}{2}\hat{\epsilon}\,\hat{h}\,\frac{\hat{l}_e}{\hat{l}}\,\hat{V}_{\mathrm{DC}}^2\left(\frac{1+0.65\frac{(\hat{v}-\hat{d})}{\hat{h}}}{\left(\hat{v}-\hat{d}\right)^2}-\frac{1+0.65\frac{(\hat{v}+\hat{d})}{\hat{h}}}{\left(\hat{v}+\hat{d}\right)^2}\right)(H(\hat{s}-\hat{s}_1)-H(\hat{s}-\hat{s}_2))$$

where $\hat{s}_1 = (\hat{l}_b + \hat{f}_b(\hat{t}))$, $\hat{s}_2 = (\hat{l}_e + \hat{l}_b + \hat{f}_b(\hat{t}))$, $\hat{\alpha}$ represents the linear damping coefficient, $\hat{\beta}$ the quadratic damping coefficient, $\hat{E}$ elastic modulus, $\hat{I}$ second moment of area, and the boundary conditions are given by

$$\hat{v}(0,\hat{t}) = 0, \quad \hat{v}(0,\hat{t})' = 0, \quad \hat{v}(\hat{l},\hat{t})'' = 0, \quad \hat{v}(\hat{l},\hat{t})''' = 0 \tag{5}$$

$\hat{F}_{\mathrm{qd}}$ represents the nonlinear hydrodynamic or aerodynamic dissipative force due to fluid-structure interaction. For high Reynolds numbers the corresponding nonlinear damping force is proportional to the velocity squared [35]. In micro- and nano-scale the structures move at high speed and therefore including the quadratic damping in parametric resonance becomes important to improve the efficacy of a single-mode approximation, *e.g.* see [13] and [14]. For analytical analysis using the method of multiple scales, the quadratic damping term $-\hat{\beta}\,\dot{\hat{v}}|\dot{\hat{v}}|$ may be replaced with averaged quadratic damping term for one cycle, so that the parameter can be related to the equivalent viscous damping found by equating the average energy dissipation [9, 35] and the force direction is opposite to the velocity.

In equation (4), $\hat{F}_{\mathrm{ns}}$ and $\hat{F}_{\mathrm{ni}}$ represent the stiffness (geometric) and inertia nonlinearities. The nonlinear stiffness force accounts for nonlinearity in curvature and the nonlinear inertia term provides the necessary constraint force for inextensibility, *i.e.* for the neutral axis of the beam to remain inextensible.

The equation of motion is non-dimensionalised by introducing

$$\hat{v} = v\,\hat{d}, \quad \hat{s} = s\,\hat{l}, \quad \hat{t} = t\,\hat{\kappa}, \quad \hat{l}_e = l_e\,\hat{l}, \quad \hat{d} = d\,\hat{l} \tag{6}$$

The equation of motion is then recast as

$$v'''' + \ddot{v} = -\,\alpha\,\dot{v} - \beta\,\dot{v}|\dot{v}| - d^2\left(4v'v''v''' + \left(v''^3 + v'^2 v''''\right)\right)$$

$$- a_b\omega_b^2 \cos(\omega_b\, t)\left(v' - (1-s)v''\right) - \frac{1}{2}d^2\left[v'\int_1^s\left[\frac{\partial^2}{\partial t^2}\int_0^s v'^2\,\mathrm{d}s\right]\mathrm{d}s\right]'$$
$$+\ \hat{V}(\hat{t})^2\left(\frac{\nu+\nu_f\,(1-v)}{(1-v)^2} - \frac{\nu+\nu_f\,(1+v)}{(1+v)^2}\right)H_e(s,t) \tag{7}$$

Note that the length and time variables are dropped for clarity of notation, that is $v \equiv v(s,t)$. Also the prime and dot now represent differentiation with respect to non-dimensional position and time. The non-dimensional parameters are given by

$$\hat{\kappa} = \sqrt{\frac{\hat{m}\,\hat{l}^4}{\hat{E}\,\hat{I}}},\ \hat{\alpha} = \frac{\hat{E}\,\hat{I}\,\hat{\kappa}}{\hat{l}^4}\alpha,\ \hat{\beta} = \frac{\hat{E}\,\hat{I}\,\hat{\kappa}^2}{\hat{l}^4\,\hat{d}}\beta,$$
$$\hat{a}_b = \frac{\hat{E}\,\hat{I}\,\hat{\kappa}^2}{\hat{m}\,\hat{l}^3\,\hat{\omega}_b^2}a_b,\ \hat{\epsilon} = \frac{2\hat{d}^3\hat{E}\hat{I}}{\hat{h}_e\hat{l}^3\hat{l}_e}\nu,\ \hat{\epsilon}_f = \frac{2\hat{d}^2\hat{E}\hat{I}}{\hat{l}^3\hat{l}_e}\nu_f. \tag{8}$$

The coefficient $H_e(s,t) = H(s-s_1(t)) - H(s-s_2(t))$ determines if the electrostatic force $F_{es}(s,t)$ due to side electrodes is active.

3. Reduced-order model

In this work, the principal parametric resonance of a vibrational structure is investigated. In the presence of damping all modes other than directly or indirectly excited modes would be significantly damped in the steady-state response [36, 37, 38]. Hence for a carefully designed (symmetric) cantilever the modal interactions are not as strong as those for a clamped-clamped beam where internal resonance would be expected. There are various references in the literature where the experimental results of systems with a similar reduced-order model under parametric excitation are compared to the single-mode approximation, e.g. see [39], [9], [40], [14], and [41]. The results show good to excellent agreement between the single-mode analysis and experimental results (for the fundamental parametric resonance). In the examples used in this paper we have ensured, through a detailed three-dimensional finite element analysis, that the second natural frequency of the structure is sufficiently far from the first natural

frequency and twice this frequency (i.e. the modes are widely spaced). Furthermore, we have made sure the ratio of the higher resonant frequencies to the fundamental frequency and its double are not integers to reduce the possibility of modal interactions.

To derive a single-mode representation of the response of the dynamic system (7) around the initial equilibrium ($v(s,0)=0$), the response $v(s,t)$ is expressed in the form

$$v(s,t) = \phi(s)p(t) \tag{9}$$

where $\phi(s)$ and $p(t)$ indicate the mode shape and the generalized coordinate (modal coordinate) of the vibrating structure. Expanding the electrostatic force term on the right-hand side of (7) around $v=0$ using Taylor's expansion, keeping terms up to fifth-order, and substituting (9) into the result, one obtains

$$f_{es}(s,t) = 2\hat{V}_{\mathrm{DC}}^2 p(t)\phi(s)\left(\nu_f + 2\nu + \left(\nu_f + 6\nu\right)p(t)^4\phi(s)^4 + \left(\nu_f + 4\nu\right)p(t)^2\phi(s)^2\right) \tag{10}$$

To arrive at a single-mode approximation of the dynamic system, we use Galerkin's method and insert equation (9) (and (10)) into (7), multiply through by the mode shape $\phi(s)$, and integrate the resulting equation term-by-term from 0 to 1, to obtain

$$\begin{aligned}
\ddot{p}(t)\int_0^1 \phi(s)\phi(s)\,\mathrm{d}s + p(t)\int_0^1 \phi(s)\phi^{(4)}(s)\,\mathrm{d}s &= -\alpha\dot{p}(t)\int_0^1 \phi(s)\phi(s)\,\mathrm{d}s \\
&\quad - \beta\dot{p}(t)\left|\dot{p}(t)\right|\int_0^1 \phi(s)\phi(s)\phi(s)\,\mathrm{d}s + \int_0^1 \phi(s) f_{es}(s,t) H_e(s,t)\,\mathrm{d}s \\
&\quad - a_b p(t)\left(\cos\omega_b t\right)\int_0^1 \phi(s)\left((s-1)\phi''(s) + \phi'(s)\right)\mathrm{d}s \\
&\quad - \frac{1}{2}d^2 p(t)\left(\left(p(t)\ddot{p}(t) + \dot{p}(t)^2\right)\int_0^1 \phi(s)\phi'(s)\left(\int_0^s 2\phi'(s)^2\,\mathrm{d}s\right)\mathrm{d}s\right. \\
&\quad \left. + \left(p(t)\ddot{p}(t) + \dot{p}(t)^2\right)\int_0^1 \phi(s)\phi''(s)\left(\int_1^s\left(\int_0^s 2\phi'(s)^2 ds\right)\mathrm{d}s\right)\mathrm{d}s\right)
\end{aligned}$$

$$+2p(t)^2\int_0^1 \phi(s)\phi''(s)\left(\phi''(s)^2+4\phi^{(3)}(s)\phi'(s)\right)\mathrm{d}s$$
$$+2p(t)^2\int_0^1 \phi(s)\phi^{(4)}(s)\phi'(s)^2\,\mathrm{d}s\Bigg) \tag{11}$$

Employing the modes are orthonormal and grouping similar terms yields the corresponding Mathieu Hill equation for this dynamical system as

$$\begin{aligned}\ddot{p}(t)+\omega_e^2 p(t) =& -\Pi_1 a_b\omega_b^2\cos(\omega_b t)\,p(t)-\alpha\dot{p}(t)-\beta\Gamma_7\dot{p}(t)|\dot{p}(t)|\\ &+2\hat{V}_{\mathrm{DC}}^2\left(H_6(t)\left(\nu_f+6\nu\right)p(t)^2+H_4(t)\left(\nu_f+4\nu\right)\right)p(t)^3\\ &+\Pi_2 p(t)^3-\Pi_3 p(t)\dot{p}(t)^2-\Pi_3 p(t)^2\ddot{p}(t)\end{aligned} \tag{12}$$

where (assuming the fundamental mode is used in (9))

$$\omega_e^2 = \omega_1^2-2H_2(t)\hat{V}_{\mathrm{DC}}^2\left(\nu_f+2\nu\right) \tag{13}$$
$$\Pi_1 = \int_0^1 \phi_1(s)\phi_1'(s)\,\mathrm{d}s-\int_0^1 \phi_1(s)\phi_1''(s)\,\mathrm{d}s+\int_0^1 s\phi_1(s)\phi_1''(s)\,\mathrm{d}s \tag{14}$$
$$\begin{aligned}\Pi_2 =& -4d^2\int_0^1 \phi_1(s){\phi_1}^{(3)}(s)\phi_1'(s)\phi_1''(s)\,\mathrm{d}s-d^2\int_0^1 \phi_1(s){\phi_1}^{(4)}(s)\phi_1'(s)^2\,\mathrm{d}s\\ &-d^2\int_0^1 \phi_1(s)\phi_1''(s)^3\,\mathrm{d}s\end{aligned} \tag{15}$$
$$\begin{aligned}\Pi_3 =& d^2\int_0^1 \phi_1(s)\phi_1''(s)\left(\int_1^s\left(\int_0^s \phi_1'(s)^2\,\mathrm{d}s\right)\mathrm{d}s\right)\mathrm{d}s\\ &+d^2\int_0^1 \phi_1(s)\phi_1'(s)\left(\int_0^s \phi_1'(s)^2\,\mathrm{d}s\right)\mathrm{d}s\end{aligned} \tag{16}$$

$$\begin{aligned}H_2(t) =& \int_{s_1(t)}^{s_2(t)}\phi(s)f_{es}(s,t)\,\mathrm{d}s\\ =& H_{2,0}+H_{2,1}a_b\left(\cos\omega_b t\right)+H_{2,2}a_b^2\left(\cos\omega_b t\right)^2+H_{2,3}a_b^3\left(\cos\omega_b t\right)^3\end{aligned} \tag{17}$$
$$\begin{aligned}H_4(t) =& \int_{s_1(t)}^{s_2(t)}\phi(s)f_{es}(s,t)\,\mathrm{d}s\\ =& H_{4,0}+H_{4,1}a_b\left(\cos\omega_b t\right)+H_{4,2}a_b^2\left(\cos\omega_b t\right)^2+H_{4,3}a_b^3\left(\cos\omega_b t\right)^3\end{aligned} \tag{18}$$
$$\begin{aligned}H_6(t) =& \int_{s_1(t)}^{s_2(t)}\phi(s)f_{es}(s,t)\,\mathrm{d}s\\ =& H_{6,0}+H_{6,1}a_b\left(\cos\omega_b t\right)+H_{6,2}a_b^2\left(\cos\omega_b t\right)^2+H_{6,3}a_b^3\left(\cos\omega_b t\right)^3\end{aligned} \tag{19}$$

The $H_{i,j}$ terms for $i = 2, 4, 6, j = 0, 1, 2, 3$ are lengthy expressions including the system parameters and the fundamental vibrational mode shape of the cantilever resonator. $\hat{\omega}_1 = (1.875)^2$ represents the fundamental free vibrational frequency of the cantilever resonator.

The coefficients of equation (12) are evaluated using the fundamental mode-shape of the cantilever beam. The nth mode shape is given by

$$\phi_n = c_n \left(\frac{\sin(\lambda) - \sinh(\lambda)}{\cosh(\lambda) + \cos(\lambda)} \left(\sinh(\lambda\, s) - \sin(\lambda\, s) \right) + \cosh(\lambda\, s) - \cos(\lambda\, s) \right) \tag{20}$$

where the λ's are the eigenvalues of the cantilever beam found by computing the roots of $1 + \cos(\lambda)\cosh(\lambda) = 0$ and c_n normalizes the eigenfunctions such that $\int_0^1 \phi_m(s)\phi_n(s)\,\mathrm{d}s = \delta_{m,n}$ where $\delta_{m,n} = 1$ for $m = n$ and $\delta_{m,n} = 0$ for $m \neq n$. Here we use the first mode, and therefore have $\int_0^1 \phi_1^2(s)\,\mathrm{d}s = 1$.

4. Perturbation analysis

We are interested in studying the behavior of the dynamic system when the excitation frequency is near two-times the fundamental natural frequency of system ($\omega_b \approx 2\omega_e$). A uniform second-order approximation of the response is defined using the method of multiple scales where the generalized coordinate is expressed as a series of the form

$$p(t) = \epsilon\, p_1(t_0, t_1, t_2) + \epsilon^2 p_2(t_0, t_1, t_2) + \epsilon^3 p_3(t_0, t_1, t_2) \tag{21}$$

where the time scales are defined as $t_0 = t$, $t_1 = \epsilon\, t$, and $t_2 = \epsilon^2 t$. The parameter ϵ does not indicate anything other than the order of terms [35, 42]. The base excitation amplitude, the linear damping coefficient, and the quadratic damping coefficients will be scaled by ϵ, ϵ^2, and ϵ respectively.

Inserting equation (21) into (12), collecting the coefficients of like powers of ϵ up to the third-order, and neglecting higher order terms results in the following sequence of equations:

- $\mathcal{O}(\epsilon^1)$:

$$\partial_0^2 p_1 + \omega_e^2 p_1 = 0 \tag{22}$$

- $\mathcal{O}(\epsilon^2)$:

$$\partial_0^2 p_2 + \omega_e^2 p_2 = -2\partial_1\partial_0 p_1 - 4a_b\Pi_1\omega_e^2\cos(\omega_b t)p_1 \tag{23}$$

- $\mathcal{O}(\epsilon^3)$:

$$\begin{aligned}\partial_0^2 p_3 + \omega_e^2 p_3 = & -2\partial_2\partial_0 p_1 - 2\partial_1\partial_0 p_2 - \partial_1^2 p_1 \\ & - 4\Pi_1 a_b\omega_e^2\cos(\omega_b t)\, p_2 + 2H_{4,0}\hat{V}_{\mathrm{DC}}^2\left(\nu_f + 4\nu\right) p_1^3 + \Pi_2 p_1^3 \\ & - \partial_0 p_1\left(\alpha + \beta\Gamma_7\,|\partial_0 p_1|\right) - \Pi_3 p_1\,\partial_0 {p_1}^2 - \Pi_3 p_1^2\,\partial_0^2 p_1\end{aligned} \tag{24}$$

where ∂_m^n indicates the nth derivative with respect to the mth time scale, that is t_m, for $m = 0, 1, 2$. The arguments of functions, (t_0, t_1, t_2) and (t_1, t_2), are removed for compactness of notation. Equation (22) represents a linear eigenvalue problem admitting a solution in the exponential form

$$p_1(t_0, t_1, t_2) = \bar{A}(t_1, t_2)\, e^{-it_0\omega_e} + A(t_1, t_2)\, e^{it_0\omega_e} \tag{25}$$

where $A(t_1, t_2)$ and its complex conjugate $\bar{A}(t_1, t_2)$ are to be determined by removing secular terms in computing the solutions of the second-order $\mathcal{O}(\epsilon^2)$ and the third-order $\mathcal{O}(\epsilon^3)$ problems. Substituting equation (25) into (23) and introducing $\omega_b = 2\omega_e + 2\sigma\epsilon$, where σ represents the nearness of the two frequencies, the solvability equations of the second-order are found by setting the coefficients of the secular terms, $e^{-it_0\omega_e}$ and $e^{it_0\omega_e}$, equal to zero:

$$i\omega_e\partial_1 A(t_1, t_2) + \Pi_1 a_b\omega_e^2 e^{2i\sigma t_1}\bar{A}(t_1, t_2) = 0 \tag{26}$$

$$i\omega_e\partial_1\bar{A}(t_1, t_2) - \Pi_1 a_b\omega_e^2 e^{-2i\sigma t_1} A(t_1, t_2) = 0 \tag{27}$$

where the second equation is the complex conjugate of the first one and automatically satisfied for the solution of the first one. Introducing (25) into (23), and eliminating secular terms using (26)-(26), (23) is solved for the particular solution

$$p_2(t_0, t_1, t_2) = \frac{\Pi_1 a_b}{4}\left(A(t_1, t_2)\, e^{it_0(\omega_b+\omega_e)} + \bar{A}(t_1, t_2)\, e^{-it_0(\omega_b+\omega_e)}\right) \tag{28}$$

Substitution of equations (25) and (28) into the third-order problem $\mathcal{O}(\epsilon^3)$, and collecting secular and small divisor terms results in the following solvability equation:

$$\begin{aligned}\partial_1^2 A(t_1,t_2) + 2i\omega_e \partial_2 A(t_1,t_2) = \\ -\frac{1}{2}a_b^2\Pi_1^2\omega_e^2 A(t_1,t_2) + 4(6\nu+\nu_f)H_{4,0}\hat{V}_{\mathrm{DC}}^2 A(t_1,t_2)^2\bar{A}(t_1,t_2) \\ + 2\Pi_3\omega_e^2 A(t_1,t_2)^2\bar{A}(t_1,t_2) + 3\Pi_2 A(t_1,t_2)^2\bar{A}(t_1,t_2) \\ - i\alpha\omega_e A(t_1,t_2) - \beta\Gamma_7 f_d(A,\bar{A})\end{aligned} \tag{29}$$

where, to derive an analytical form of the quadratic damping term, the corresponding term is expanded in a Fourier series as

$$\partial_0 p_1 \ |\partial_0 p_1| = \sum_{n=-\infty}^{\infty} f_n(A,\bar{A}) e^{in\omega_e t_0}. \tag{30}$$

The first term generates the secular term:

$$\partial_0 p_1 \ |\partial_0 p_1| = f_d(A,\bar{A}) e^{i\omega_e t_0} + \bar{f}_d(A,\bar{A}) e^{-i\omega_e t_0} \tag{31}$$

where f_1 and f_{-1} have been replaced with f_d and $\bar{f}_d$. Note that the coefficients of $e^{-i\omega_e t_0}$ produces the complex conjugate of (29) and is automatically satisfied for solutions of (29). To further remove $\partial_1^2 A(t_1,t_2)$ and simplify equation (29), we differentiate (26) with respect to t_1 and substitute into equation (29) along with equation (27) to arrive at

$$\begin{aligned}2i\omega_e\partial_2 A(t_1,t_2) =& 3\left(\Pi_2 + 2(4\nu+\nu_f)H_{4,0}\hat{V}_{\mathrm{DC}}^2\right) A(t_1,t_2)^2\bar{A}(t_1,t_2) \\ &+ 2\Pi_3\omega_e^2 A(t_1,t_2)^2\bar{A}(t_1,t_2) - i\alpha\omega_e A(t_1,t_2) - \beta\Gamma_7 f_d(A,\bar{A}) \\ &+ 2\Pi_1\sigma\omega_e a_b e^{2i\sigma t_1}\bar{A}(t_1,t_2) - \frac{3}{2}\Pi_1^2\omega_e^2 a_b^2 A(t_1,t_2)\end{aligned} \tag{32}$$

Equations (26) and (32) represent differentiating $A(t_1,t_2)$ with respect to its variables and may be combined using the method of reconstitution [43, 44] to arrive at the following solvability condition

$$\begin{aligned}&2i\omega_e A'(t) + A(t)\left(i\alpha\omega_e + \frac{3}{2}a_b^2\Pi_1^2\omega_e^2\right) - 2\Pi_1 a_b\omega_e e^{2i\sigma t}\left(\sigma-\omega_e\right) \\ &- A(t)^2\overline{A}(t)\left(6H_{4,0}\hat{V}_{\mathrm{DC}}^2\left(\nu_f+4\nu\right) + 2\Pi_3\omega_e^2 + 3\Pi_2\right) + \beta\Gamma_7 f_d(A,\bar{A}) = 0\end{aligned} \tag{33}$$

To separate the solvability equation into two real equations we can either assume

$$A(t) = \frac{1}{2}(A_r(t) + iA_i(t))e^{i\sigma t}, \;\; \overline{A}(t) = \frac{1}{2}\left(A_r(t) - iA_i(t)\right)e^{-i\sigma t} \tag{34}$$

to obtain the modulation equations in Cartesian form or

$$A(t) = \frac{1}{2}a_p(t)e^{i\theta_p(t)}, \;\; \overline{A}(t) = \frac{1}{2}a_p(t)e^{-i\theta_p(t)} \tag{35}$$

to arrive at the modulation equations in polar coordinates. To derive an analytical form of quadratic damping, we compute f_d, see equations (30) and (31), using a Fourier series. To this end, note that

$$f_d(A, \bar{A}) = \frac{1}{2\pi}\int_0^{2\pi} e^{-i\tau}\partial_0 p_1 \; |\partial_0 p_1| \, \mathrm{d}\tau \tag{36}$$

where $\tau = \omega_e t_0$. Substituting (25), (34) and (35) into (36), and performing the integration we compute the analytical form of the quadratic damping to be

$$f_d(A, \bar{A}) = \frac{4i\omega_e^2(A_r(t) + iA_i(t))\sqrt{A_i(t)^2 + A_r(t)^2}e^{i\sigma t}}{3\pi} \tag{37}$$

$$f_d(A, \bar{A}) = \frac{4i\beta\Gamma_7\epsilon^2 a_p^2(t)\omega_e^2}{3\pi} \tag{38}$$

in Cartesian and polar coordinates, respectively. Substituting (34), (35), (37), and (38) into (33), separating the real and imaginary terms, and setting each group equal to zero results in modulation equations

$$\begin{aligned} &A_i'(t) + A_r(t)\left(\sigma - \Pi_1 a_b\omega_e\right) + A_r(t)\left(\Pi_1\sigma a_b - \frac{3}{4}\Pi_1^2 a_b^2\omega_e\right) \\ &\quad + A_i(t)\left(\frac{4\beta\Gamma_7\omega_e\sqrt{A_i(t)^2 + A_r(t)^2}}{3\pi} + \frac{\alpha}{2}\right) \\ &\quad + \frac{\mu}{\omega_e}\left(A_i(t)^2 A_r(t) + A_r(t)^3\right) = 0 \end{aligned} \tag{39}$$

$$\begin{aligned} &A_r'(t) - A_i(t)\left(\Pi_1 a_b\omega_e + \sigma\right) + A_i(t)\left(\Pi_1\sigma a_b + \frac{3}{4}\Pi_1^2 a_b^2\omega_e\right) \\ &+ A_r(t)\left(\frac{4\beta\Gamma_7\omega_e\sqrt{A_i(t)^2 + A_r(t)^2}}{3\pi} + \frac{\alpha}{2}\right) \\ &- \frac{\mu}{\omega_e}\left(A_i(t)^3 - A_i(t)A_r(t)^2\right) = 0 \end{aligned} \tag{40}$$

in Cartesian coordinates, and

$$a_p(t)\eta_p'(t) = \left(\sigma - \Pi_1 a_b \omega_e \cos\left(2\eta_p(t)\right)\right) a_p(t) + \left(\Pi_1 \sigma a_b \cos\left(2\eta_p(t)\right) - \frac{3}{4}\Pi_1^2 a_b^2 \omega_e\right) a_p(t) + \frac{\mu}{\omega_e} a_p(t)^3 \tag{41}$$

$$a_p'(t) = \left(\Pi_1 \sigma a_b \sin\left(2\eta_p(t)\right) - \frac{4\beta\Gamma_7 \omega_e a_p(t)}{3\pi} - \frac{\alpha}{2}\right) a_p(t) - \Pi_1 a_b \omega_e \sin\left(2\eta_p(t)\right) a_p(t) \tag{42}$$

in polar coordinates. The constant $\mu = \frac{1}{8}\left(6H_{4,0}\hat{V}_{\mathrm{DC}}^2\left(\nu_f + 4\nu\right) + 2\Pi_3\omega_e^2 + 3\Pi_2\right)$. The general solution for the modal coordinate is obtained by inserting equations (25) and (28) into (21) (and setting the scaling parameter ϵ to 1)

$$p(t) = a_p(t)\cos\left(\frac{\omega_b t}{2} - \eta_p(t)\right) + \frac{1}{4}\Pi_1 a_b a_p(t)\cos\left(\frac{3\omega_b t}{2} - \eta_p(t)\right) \tag{43}$$

which is then projected back to the actual displacement space using equations (9) and (6). The dynamic equilibrium solutions or steady-state response corresponds to $a_p'(t) = 0$ and $\eta_p'(t) = 0$. Therefore, we compute the equilibrium solutions and their stability and plot them on frequency-response and force-response curves to investigate the dynamic system under the principal parametric excitation ($\omega_b \approx 2\omega_e$).

Setting $a_p'(t)$ and $\eta_p'(t)$ equal to zero in equations (41)-(42), the resulting equations are solved for $\cos\left(2\eta_p(t)\right)$ and $\sin\left(2\eta_p(t)\right)$ and combined using the trigonometric identity, $\sin\left(2\eta_p(t)\right)^2 + \cos\left(2\eta_p(t)\right)^2 = 1$, to obtain the amplitude equation:

$$\gamma_{1,1} a_p(t)^4 + \gamma_{1,2} a_p(t)^2 + \gamma_{1,3} a_p(t) + \gamma_{1,4} = 0 \tag{44}$$

where

$$\gamma_{1,1} = 9\pi^2\left(6H_{4,0}\hat{V}_{\mathrm{DC}}^2\left(\nu_f + 4\nu\right) + 2\Pi_3\omega_e^2 + 3\Pi_3\right)^2$$

$$\gamma_{1,2} = 36\pi^2\omega_e\left(4\sigma - 3\Pi_1^2 a_b^2\omega_e\right)\left(6H_{4,0}\hat{V}_{\mathrm{DC}}^2\left(\nu_f + 4\nu\right) + 2\Pi_3\omega_e^2 + 3\Pi_2\right) + 1024\beta^2\Gamma_7^2\omega_e^4$$

$$\gamma_{1,3} = 768\pi\alpha\beta\Gamma_7\omega_e^3$$

$$\gamma_{1,4} = 144\pi^2\alpha^2\omega_e^2 - 36\pi^2\omega_e^2\left(\Pi_1^2 a_b^2\left(\omega_e^2\left(16 - 9\Pi_2^2 a_b^2\right) - 8\sigma\omega_e + 16\sigma^2\right) - 16\sigma^2\right)$$

For the phase equation, after setting $a_p'(t) = 0$ and $\eta_p'(t) = 0$, we solve equation (42) for $a_p(t)$ and substitute the resulting expression into equation (41) to obtain

$$\gamma_{2,1}\sin^3(2\eta) + \gamma_{2,2}\sin^2(2\eta) + \gamma_{2,3}\sin(2\eta) + \gamma_{2,4}\sin(2\eta)\cos(2\eta) + \gamma_{2,5}\cos(2\eta) + \gamma_{2,6} = 0 \tag{45}$$

where

$$\begin{aligned}
\gamma_{2,1} =& \frac{27}{512}\pi^3\Pi_1^3 a_b^3\left(\sigma-\omega_e\right)^3\left(6H_{4,0}\hat{V}_{\mathrm{DC}}^2\left(\nu_f+4\nu\right)+2\Pi_3\omega_e^2+3\Pi_2\right)\\
\gamma_{2,2} =& -\frac{81\pi^3\alpha\Pi_1^2 a_b^2\left(\sigma-\omega_e\right)^2\left(6H_{4,0}\hat{V}_{\mathrm{DC}}^2\left(\nu_f+4\nu\right)+2\Pi_3\omega_e^2+3\Pi_2\right)}{1024}\\
\gamma_{2,3} =& \frac{3\pi\Pi_1 a_b\left(\sigma-\omega_e\right)\left(81\pi^2\alpha^2\Pi_2+128\beta^2\Gamma_7^2\omega_e^3\left(4\sigma-3\Pi_1^2 a_b^2\omega_e\right)+54\pi^2\alpha^2\Pi_3\omega_e^2\right)}{2048}\\
&+\frac{3\pi\Pi_1 a_b\left(\sigma-\omega_e\right)\left(162\pi^2\alpha^2 H_{4,0}\hat{V}_{\mathrm{DC}}^2\left(\nu_f+4\nu\right)\right)}{2048}\\
\gamma_{2,4} =& \frac{3}{4}\pi\beta^2\Gamma_7^2\Pi_1^2 a_b^2\omega_e^3\left(\sigma-\omega_e\right)^2\\
\gamma_{2,5} =& \frac{3}{8}\pi\alpha\beta^2\Gamma_7^2\Pi_1 a_b\omega_e^3\left(\omega_e-\sigma\right)\\
\gamma_{2,6} =& -\frac{3}{512}\pi\alpha\left(\frac{9}{8}\pi^2\alpha^2\left(6H_{4,0}\hat{V}_{\mathrm{DC}}^2\left(\nu_f+4\nu\right)+2\Pi_3\omega_e^2+3\Pi_2\right)\right)\\
&+\frac{3}{512}\pi\alpha\left(48\beta^2\Gamma_7^2\Pi_1^2 a_b^2\omega_e^4-64\beta^2\Gamma_7^2\sigma\omega_e^3\right)
\end{aligned}$$

To examine the stability of fixed points, we compute the Jacobian matrix for (41)-(42) and its corresponding eigenvalues. For the unstable branch of the frequency-response curve the eigenvalues are real and for the stable branch the eigenvalues are complex with negative real parts. To obtain the instability threshold for the trivial solution, that is the boundaries of the Arnold tongue, we set $\eta_p'(t_2) = 0$, $a_p'(t_2) = 0$ obtaining (24) and $a_p(t_2) = 0$ for the trivial solution in (44), and find the following relation between the detuning parameter σ and

the excitation amplitude a_b:

$$4\left(\alpha^2+4\sigma^2\right)+\Pi_1^2 a_b^2\left(\omega_e^2\left(9\Pi_1^2 a_b^2-16\right)+8\sigma\omega_e-16\sigma^2\right)=0 \qquad (46)$$

Plotting this parametric equation in the $\sigma-a_b$ plane indicates the boundaries for the instability of the trivial solution. From (13)-(14) and (46) one notes that the DC voltage, the mode-shape, and the linear damping α affect the instability threshold. The area between the tongue and the horizontal frequency (the detuning) axis represent the stable region.

5. Case study: a resonator

Parametric resonance offers characteristics other than the amplitude and phase of the response where the frequency-response abruptly switches from the trivial zero-equilibrium to a nontrivial non-zero response through a supercritical pitchfork bifurcation. Micro- and nano-electromechanical-systems (MEMS and NEMS) offer significant value to developing new technologies for sensors, switches, resonators, filters, and antennas. Following a commercialized SOI-MUMPS process [45], a resonator is designed with the dimensions given in Table 1. One can employ a comb-drive or a parallel-plate actuator to excite the base (primary) resonator, see Figure 1. The resonator's motion is detected by the two side electrodes creating a differential capacitor. The motion (displacement) translates to an induced current going through a trans-impedance circuit consisting a resistor (gain) to output the voltage [46]. Closed-form expressions are available in the literature to compute the sense current from the displacement for arbitrary large motions using parallel-plate capacitors. The non-dimensional parameters are computed using relations (10) and limiting the base excitation amplitude to less than 1μm (2% of electrode length) coefficients of electrostatic pull forces are reasonably truncated to the their first-order constant approximations in (17)-(19).

Before discussing the non-linear response, to improve and optimize the design, identify modal frequencies, and minimize the effect of modal interaction, a

Table 1: Dimensions and parameters of the resonator

$\hat{l}$	$\hat{t}$	$\hat{w}$	$\hat{d}$	$\hat{E}$	$\hat{\rho}$
$500\,\mu$m	$25\,\mu$m	$5\,\mu$m	$1\,\mu$m	169 GPa	$2330\,\mathrm{kg/m^3}$
$\hat{\epsilon}$	$\hat{\epsilon}_f$	$\hat{h}$	$\hat{l}_e$	$\hat{l}_b$	$\hat{V}_{\mathrm{DC}}$
$8.854\times10^{-12}\,\mathrm{F/m}$	$0.65\times8.854\times10^{-12}\,\mathrm{F/m}$	$25\,\mu$m	$400\,\mu$m	$100\,\mu$m	1 V

preliminary linear three-dimensional finite element analysis is performed. The fundamental (first) mode of structure is the in-plane bending of the sense (cantilever) beam in the z direction and its modal frequency is 27.519 kHz, the second mode is the in-plane bending of the base resonator in the x direction with a modal frequency of 62.846 kHz, the third mode of the structure is the out-of-plane bending of the sense (cantilever) beam in the y direction with a modal frequency of 94.765 kHz, the fourth mode of the structure is the in-plane bending of the sense (cantilever) beam in the z direction with a modal frequency of 172.380 kHz (the second mode of the cantilever resonator), the fifth mode of the structure is an out-of-plane mode, and the sixth mode is also an out-of-plane mode. Also note that in this work we consider a PPR, however the design can be optimized for auto-parametric resonance which has been shown to have other advantages [47, 26].

It is common to use quality factor instead of damping among the M/NEMS community. The linear damping coefficient α is related to the natural frequency and quality factor through $\alpha = \frac{\omega}{Q_F}$ and the quadratic damping coefficient range is in the same order of magnitude as examined in [14]. To start our analysis, the linear damping parameter α is varied and the instability threshold (Arnold Tongue) is computed and plotted in the $a_b - \sigma$ plane in Figures 3a-3b. Increasing the damping pushes the curve up and expands the stable region under the curve, however far from the principal parametric resonance condition damping plays an insignificant role in changing the stability of the dynamic system.

The linear and nonlinear (quadratic) damping play considerable roles in changing the quantitative and qualitative behaviour of system response. Setting

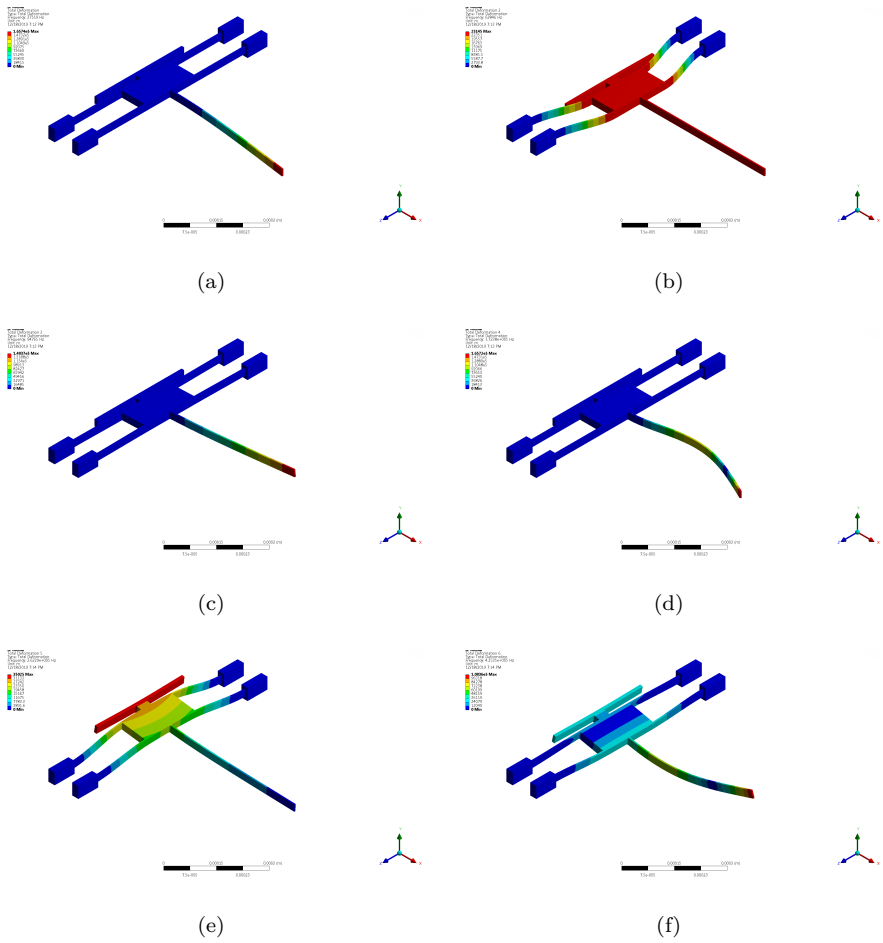

Figure 2: The (a) first, (b) second, (c) third, (d) fourth, (e) fifth, and (f) sixth modes of the structure using three-dimensional finite element analysis.

$\beta = 0.05$ and $a_b = 0.001$ and varying the linear damping, we compute and plot the frequency-response curves for $\alpha = 0.001$ and 0.005 in Figure 4a. The black dashed-line represents the backbone curve and other dashed lines represent the unstable branches of the response. The numerical solution of the reduced-order model of (12) is computed using a fourth-order Runge-Kutta method and plotted using meshed lines. The analytical (perturbation) solution agrees with the model until the higher-order nonlinearities become significant. The nontrivial

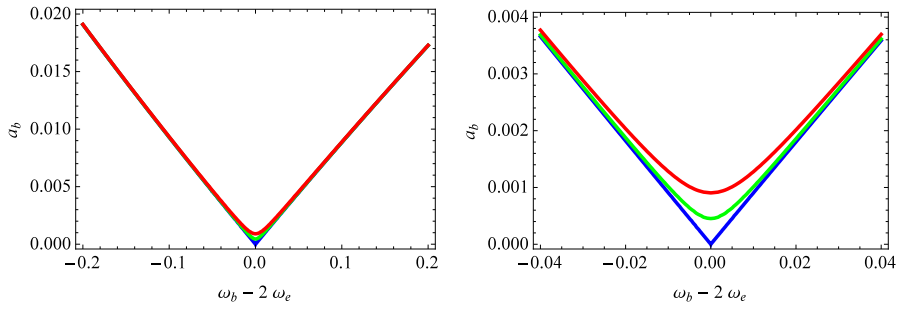

Figure 3: The stability boundaries in the $a_b - \sigma$ plane ($\alpha = 0$: blue curve, $\alpha = 0.005$: green curve, and $\alpha = 0.01$: red curve). Plot (b) is a magnified representation of plot (a) for a smaller range near zero.

stable response goes through a fold bifurcation and loses its stability at the far right end. Once we are located on an unstable orbit, a small perturbation may force the response to jump to the larger stable orbit or the trivial stable equilibrium. For the varying quadratic damping in Figure 4b, zero quadratic damping (the blue line) produces two isolated stable and unstable response branches (for the domain of interest) and for the largest β the nontrivial response is totally stable and approaches a linear system response.

To further analyze the response for an excitation amplitude sweep (a_b) and a varying quadratic damping parameter, we consider two cases where the detuning parameter is negative in Figure 5a, that is $\omega_b - 2\omega_e = -0.02$, and positive in Figure 5b, $\omega_b - 2\omega_e = 0.02$. For the negative detuning parameter, the response grows (nonlinearly) as the excitation amplitude becomes larger while for a positive detuning parameter a small quadratic damping (the blue curve $\beta = 0$) results in observing a pitchfork (from trivial to nontrivial equilibrium points) and a saddle-node bifurcation (from nontrivial stable/unstable to unstable/stable fixed points). Note that both frequency and force-response curve show that the numerical and analytical solutions are identical for $p_0 \approx 0.025$.

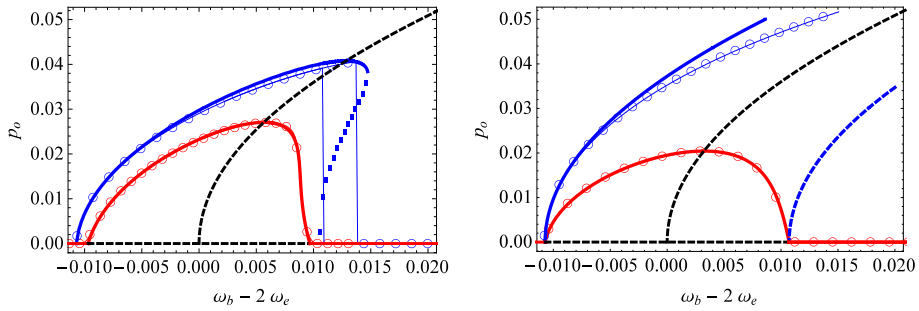

Figure 4: The frequency-response curves: (a) $a_b = 0.001$, and $\beta = 0.05$ ($\alpha = 0.001$: blue curve, and $\alpha = 0.005$: red curve). (b) $a_b = 0.001$, and $\alpha = 0.002$ ($\beta = 0$: blue curve, and $\beta = 0.1$: red curve). The black-dashed lines indicate the unstable branches/equilibrium points and the backbone curve. The (meshed) thin lines represent the numerical solution of the reduced order model and the thick lines represent the perturbation solution.

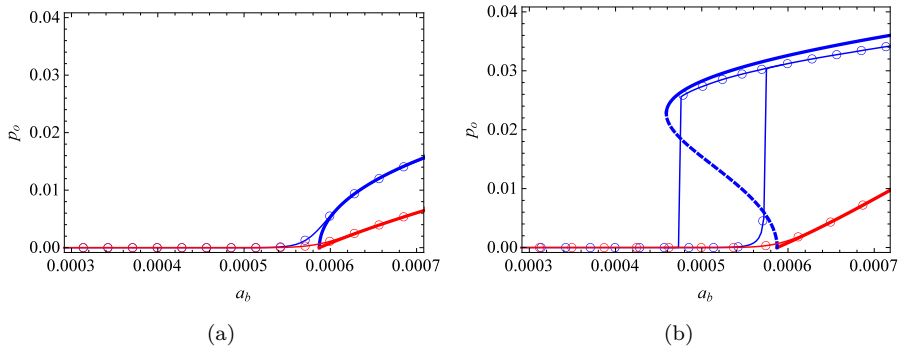

Figure 5: The frequency-response curves for $\alpha = 0.005$ and ($\beta = 0$: blue curve and $\beta = 0.05$: red curve). (a) $\omega_b - 2\omega_e = -0.004$ (b) $\omega_b - 2\omega_e = 0.004$. The meshed lines represent the numerical solution of the reduced order model and the thick lines represent the perturbation solution.

6. Acceleration/Shock/Impact measurement

Learning from our initial analysis we carefully design the parameters of the system such that by limiting the response the resonator operates in the linear

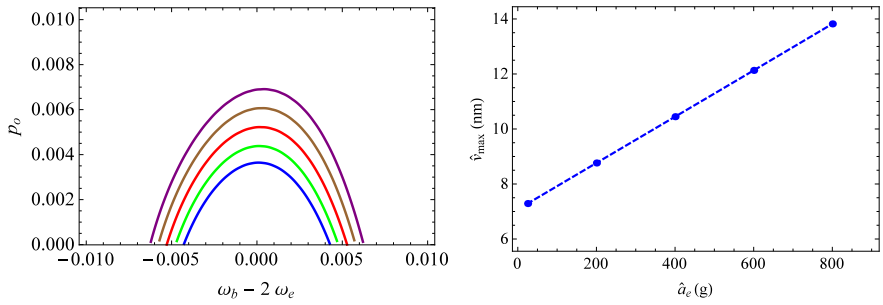

Figure 6: (a) The frequency-response curves (the non-trivial fixed points) computed from the reduced-order model and maximum amplitude (calibration) curve for increasing external acceleration $\alpha = 0.005$, $\beta = 0.1$ and $a_b = 0.0006$ ($\hat{a}_b = 300$nm).

regime. Presenting the results in dimensional form, we provide tangible evidence of the sensitivity of the inertial sensor. The base-excitation pushes the dynamic system towards bifurcating and jumping to the nontrivial solution and the external excitation (the desired acceleration) further amplifies the response. For an external acceleration with a high-frequency content and an external acceleration with a low-frequency content (which applies to most applications), the maximum amplitude and the frequency-shift methods are used to characterize the input.

6.1. High frequency external acceleration

A high frequency external acceleration modifies the amplitude of excitation, and therefore modifying the equation of motion and the corresponding reduced-order model as,

$$\begin{aligned}\ddot{p}(t) + \omega_e^2 p(t) = &- \Pi_1(a_e + 4a_b\omega_e^2)\cos(\omega_b\, t)\, p(t) - \alpha\dot{p}(t) - \beta\Gamma_7\dot{p}(t)|\dot{p}(t)| \\ &+ 2\hat{V}_{\mathrm{DC}}^2\left(H_6(t)\left(\nu_f + 6\nu\right)p(t)^2 + H_4(t)\left(\nu_f + 4\nu\right)\right)p(t)^3 \\ &+ \Pi_2 p(t)^3 - \Pi_3 p(t)\dot{p}(t)^2 - \Pi_3 p(t)^2\ddot{p}(t) \qquad (47)\end{aligned}$$

Scaling the external acceleration with $\epsilon^2 a_e$, which is consistent with the fact that the external acceleration is significantly smaller than the base-acceleration

$a_b\omega_b^2$, the amplitude and phase equations in polar coordinates become:

$$\begin{aligned} a_p(t)\eta_p'(t) =& \frac{1}{8\omega_e}a_p(t)^3\left(6H_{4,0}\hat{V}_{\mathrm{DC}}^2\left(\nu_f+4\nu\right)+2\Pi_3\omega_e^2+3\Pi_2\right) \\ &-\frac{1}{4\omega_e}\Pi_1\left(3\Pi_1 a_b^2\omega_e^2-4\sigma a_b\omega_e\cos\left(2\eta_p(t)\right)+a_e\cos\left(2\eta_p(t)\right)\right)a_p(t) \\ &+\left(\sigma-\Pi_1 a_b\omega_e\cos\left(2\eta_p(t)\right)\right)a_p(t) \end{aligned} \tag{48}$$

$$\begin{aligned} \omega_e a_p'(t) =& -\frac{1}{2}\left(\alpha\omega_e+\frac{1}{2}a_e\Pi_1\sin\left(2\eta_p(t)\right)-2\Pi_1\sigma\, a_b\,\omega_e\sin\left(2\eta_p(t)\right)\right)a_p(t) \\ &-\frac{4\Gamma_7\omega_e^2\,\beta}{3\pi}a_p(t)^2-\Pi_1 a_b\omega_e^2\sin\left(2\eta_p(t)\right)a_p(t) \end{aligned} \tag{49}$$

Setting $a_p'(t)$ and $\eta_p'(t)$ equal to zero (for a steady-state solution) in equations (48)-(49), the resulting equations are solved for $\cos\left(2\eta_p(t)\right)$ and $\sin\left(2\eta_p(t)\right)$ and combined using the trigonometric identity, $\sin\left(2\eta_p(t)\right)^2+\cos\left(2\eta_p(t)\right)^2=1$, to obtain the amplitude equation:

$$\gamma_{1,1}a_p(t)^4+\gamma_{1,2}a_p(t)^2+\gamma_{1,3}a_p(t)+\gamma_{1,4}=0 \tag{50}$$

where

$$\begin{aligned} \gamma_{1,1} =& 9\pi^2\left(6H_{4,0}\hat{V}_{\mathrm{DC}}^2\left(\nu_f+4\nu\right)+2\Pi_3\omega_e^2+3\Pi_2\right)^2 \\ \gamma_{1,2} =& 36\pi^2\omega_e\left(4\sigma-3\Pi_1^2 a_b^2\omega_e\right)\left(6H_{4,0}\hat{V}_{\mathrm{DC}}^2\left(\nu_f+4\nu\right)+2\Pi_3\omega_e^2+3\Pi_2\right) \\ &+1024\beta^2\Gamma_7^2\omega_e^4 \end{aligned} \tag{51}$$

$$\gamma_{1,3} = 768\pi\alpha\beta\Gamma_7\omega_e^3 \tag{52}$$

$$\begin{aligned} \gamma_{1,4} =& 144\pi^2\alpha^2\omega_e^2-36\pi^2\left(\Pi_1\left(a_b\omega_e\left(\omega_e\left(4-3\Pi_1 a_b\right)-4\sigma\right)+\mathrm{ae}\right)+4\sigma\omega_e\right) \\ &\left(\Pi_1\left(a_b\omega_e\left(\omega_e\left(3\Pi_1 a_b+4\right)-4\sigma\right)+a_e\right)-4\sigma\omega_e\right) \end{aligned} \tag{53}$$

A similar procedure as for (45) can be followed to obtain the phase equation. Adjusting the base-excitation amplitude (that is the amplitude of PE) and therefore the applied base-acceleration we can limit the response to the linear response. In Figures 6a-6b, the frequency-response curves and the sensitivity curve are plotted for an increasing external acceleration amplitude. Note that a

300 nm base-excitation amplitude results in ≈ 7 to ≈ 14 nm response. Most commercial silicon-based acceleration/shock sensors are limited in dynamic range to less than $\pm 24\,g$ (where g indicates the gravitational acceleration) and/or cover a limited higher range up to $500g$ [48]. Further adjusting the base-excitation amplitude, we can detect larger external accelerations and essentially use the same sensor for every application from the automotive industry, e.g. for airbags, to the aerospace industry.

Limiting the base-excitation amplitude to 100 nm, the external acceleration/shock/impact is increased from $2000\,g$ to $4000\,g$ and the frequency-response curves and the response amplitude are plotted in Figures 7a-7b. Not that $\alpha = 0.005$ damping corresponds to a quality factor of ≈ 700 which is not hard or costly to achieve for M/NEMS devices by adjusting the internal pressure during the packaging of the device.

6.2. Low frequency external acceleration

For most applications, the frequency content of the acceleration is significantly lower than the effective resonance (natural) frequency of the microstructure justifying the assumption of a constant force. The analytical natural

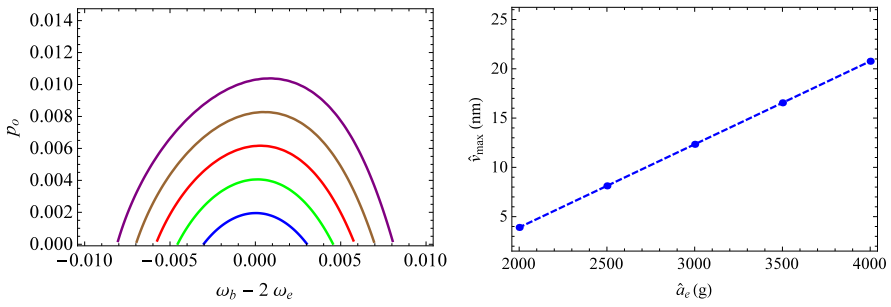

Figure 7: (a) The frequency-response curves (the non-trivial fixed points) computed from the reduced-order model and maximum amplitude (calibration) curve for increasing external acceleration $\alpha = 0.005$, $\beta = 0.1$ and $a_b = 0.0002$ ($\hat{a}_b = 100$nm).

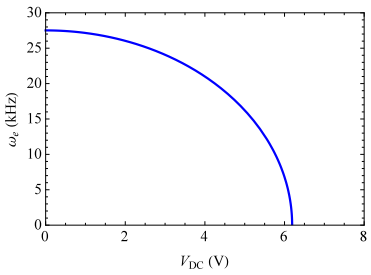

Figure 8: The effective resonance (natural) frequency curve. The static pull-in voltage is equal to 6.1915 V.

frequency of the cantilever resonator is 27.1541 kHz (at $V_{\mathrm{DC}} = 1\,\mathrm{V}$) and the DC voltage (the softening force) brings it quickly to zero for its larger values, see Figure 8. The static pull-in voltage is equal to 6.1915 V. The dynamic pull-in voltage can be up to 16 % lower than the static pull-in voltage [49, 50], however there are methods to further increase the operation range [50]. Introducing the relatively constant external acceleration into the equation of motion, we obtain the reduced-order model as,

$$\begin{aligned}\ddot{p}(t) + \omega_e^2 p(t) =& -\Pi_1(a_e + a_b\omega_b^2\cos(\omega_b t))p(t) - \alpha\dot{p}(t) - \beta\Gamma_7\dot{p}(t)|\dot{p}(t)| \\ &+ 2\hat{V}_{\mathrm{DC}}^2\left(H_6(t)\left(\nu_f + 6\nu\right)p(t)^2 + H_4(t)\left(\nu_f + 4\nu\right)\right)p(t)^3 \\ &+ \Pi_2 p(t)^3 - \Pi_3 p(t)\dot{p}(t)^2 - \Pi_3 p(t)^2\ddot{p}(t) \end{aligned} \tag{54}$$

Scaling the external acceleration with $\epsilon^2 a_e$, the modulation phase equation in polar coordinates becomes

$$\begin{aligned}a_p(t)\eta_p'(t) =& \frac{1}{8\omega_e}a_p(t)^3\left(6H_{4,0}\hat{V}_{\mathrm{DC}}^2\left(\nu_f + 4\nu\right) + 2\Pi_3\omega_e^2 + 3\Pi_2\right) \\ &- \frac{1}{4}\Pi_1\left(3\Pi_1 a_b^2\omega_e - 4\sigma a_b\cos\left(2\eta_p(t)\right) + \frac{2}{\omega_e}a_e\right)a_p(t) \\ &+ \left(\sigma - \Pi_1 a_b\omega_e\cos\left(2\eta_p(t)\right)\right)a_p(t) \end{aligned} \tag{55}$$

The amplitude equation in (42) remains unchanged indicating the amplitude may not be used to identify the external acceleration as it is not directly

affected by the external acceleration. Following a similar method as outlined earlier for equations (44), $a'_p(t)$ and $\eta'_p(t)$ are set to zero and the amplitude and phase equations are obtained. Varying the base-acceleration, the frequency-response curves and the characterization curve are plotted in Figures 9a-9b. The characterization curve demonstrates the detuning parameter for the frequency corresponding to the maximum amplitude versus the input acceleration. Note that we can also use the bifurcation points where the nontrivial solution appears and disappears or a combination of these features. It is also common to characterize the response versus the zero-input acceleration and divide the change in frequency by the initial natural frequency. Figures 10a-10b show similar results as previous figures for a set of larger shocks/impacts. The sensor can be used for even much larger values by adjusting the base-excitation amplitude, the damping, and the DC voltage. In fact, the sensor is extremely robust for the (practical case of) low-frequency external acceleration.

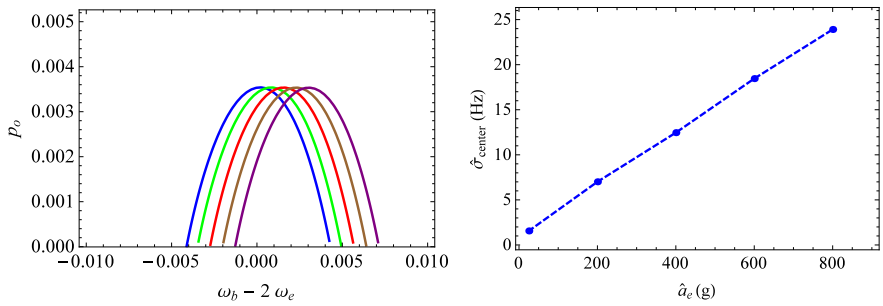

(a) (b)

Figure 9: The force-response curves (the non-trivial fixed points) and the frequency (corresponding to the maximum amplitude) curve for increasing external acceleration $\alpha = 0.005$, $\beta = 0.1$ and $a_b = 0.0006$ ($\hat{a}_b = 300$nm).

7. Conclusions

In this research, we have studied a modified generalized parametrically excited dynamic system. Including electrostatic nonlinearity into the system in-

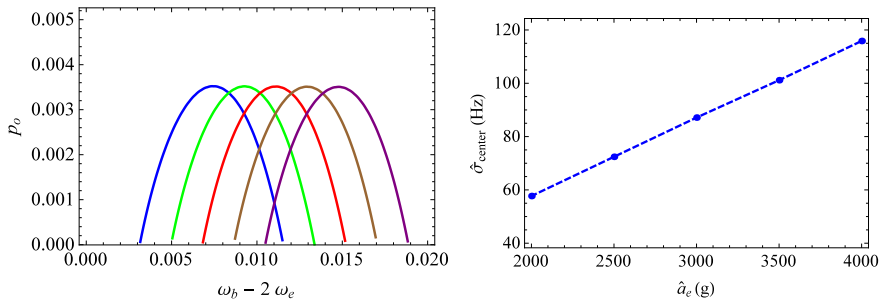

Figure 10: The force-response curves (the non-trivial fixed points) and maximum amplitude curve for increasing external acceleration $\alpha = 0.005$, $\beta = 0.1$ and $a_b = 0.0006$ ($\hat{a}_b = 300$nm).

troduces additional nonlinearities into the equation of motion and affects the backbone curve. Quadratic damping does affect the systems response and reduces/increases the number of bifurcation points. We have computed the instability threshold (Arnold tongue) and bifurcation points. We then used the dynamic system to develop an inertial measurement device. The introduction of an external acceleration term further complicates the dynamic system and its corresponding equilibrium equations. It is desired to develop linear sensors and therefore limiting the forcing term. Note that the external acceleration may be viewed as a forcing term. For PE, once the the instability threshold is passed the response grows quickly and therefore it is desired to stay near the threshold to protect the system from failure. For the parametrically excited dynamic system in this work, the sensor can be used to measure a large range of external accelerations/shock from below a hundred g to several thousand g's by adjusting the base excitation amplitude. Note that although we have not studied the importance of damping to generate the desired response, it may be used to adjust the bandwidth of the response through adjusting the internal vacuum of the device during the packaging phase.

References

[1] É. Mathieu, Memoire sur le movement vibratoire d'une membrane de forme elliptique, Journal de mathématiques pures et appliquées 2 (13) (1868) 137–203.

[2] G. W. Hill, On the part of the motion of the lunar perigee which is a function of the mean motions of the sun and moon, Acta Mathematica 8 (1) (1886) 1–36.

[3] Y. Jia, S. Du, E. Arroyo, A. A. Seshia, A micromachined device describing over a hundred orders of parametric resonance, Applied Physics Letters 112 (17) (2018) 171901.

[4] Y. Jia, S. Du, A. A. Seshia, Twenty-eight orders of parametric resonance in a microelectromechanical device for multi-band vibration energy harvesting, Scientific Reports 6 (2016) 30167.

[5] S. Shmulevich, D. Elata, A MEMS implementation of the classic meissner parametric resonator: Exploring high-order windows of unbounded response, Journal of Microelectromechanical Systems 26 (2) (2017) 325–332.

[6] L. D. Zavodney, A. Nayfeh, The non-linear response of a slender beam carrying a lumped mass to a principal parametric excitation: theory and experiment, International Journal of Non-Linear Mechanics 24 (2) (1989) 105–125.

[7] B. Balachandran, A. Nayfeh, Cyclic motions near a hopf bifurcation of a four-dimensional system, Nonlinear Dynamics 3 (1) (1992) 19–39.

[8] A. H. Nayfeh, B. Balachandran, Modal interactions in dynamical and structural systems, Applied Mechanics Reviews 42 (11S) (1989) S175–S201.

[9] T. Anderson, A. Nayfeh, B. Balachandran, Experimental verification of the importance of the nonlinear curvature in the response of a cantilever beam, Journal of Vibration and Acoustics 118 (1) (1996) 21–27.

[10] V. C. Meesala, M. R. Hajj, Parameter sensitivity of cantilever beam with tip mass to parametric excitation, Nonlinear Dynamics (2019) 1–10.

[11] L. Ng, R. Rand, Bifurcations in a Mathieu equation with cubic nonlinearities: Part II, Communications in Nonlinear Science and Numerical Simulation 7 (3) (2002) 107–121.

[12] X. Li, J. Hou, J. Chen, An analytical method for Mathieu oscillator based on method of variation of parameter, Communications in Nonlinear Science and Numerical Simulation 37 (2016) 326–353.

[13] M. Moreno-Moreno, A. Raman, J. Gomez-Herrero, R. Reifenberger, Parametric resonance based scanning probe microscopy, Applied physics letters 88 (19) (2006) 193108.

[14] G. Prakash, S. Hu, A. Raman, R. Reifenberger, Theoretical basis of parametric-resonance-based atomic force microscopy, Physical Review B 79 (9) (2009) 094304.

[15] M. F. Daqaq, R. Masana, A. Erturk, D. D. Quinn, On the role of nonlinearities in vibratory energy harvesting: a critical review and discussion, Applied Mechanics Reviews 66 (4) (2014) 040801.

[16] T. Hiller, L. L. Li, E. L. Holthoff, B. Bamieh, K. L. Turner, System identification, design, and implementation of amplitude feedback control on a nonlinear parametric MEM resonator for trace nerve agent sensing, Journal of Microelectromechanical Systems 24 (5) (2015) 1275–1284.

[17] S. A. M. Lajimi, N. Noori, A. Marzouk, B. Bahreyni, F. Golnaraghi, A novel nonlinear amplitude-modulation gyroscope incorporating internal resonance, in: Proceedings of the 25th CANCAM, 2015, pp. 1–4.

[18] P. Belardinelli, B. Sajadi, S. Lenci, F. Alijani, Global dynamics and integrity of a micro-plate pressure sensor, Communications in Nonlinear Science and Numerical Simulation 69 (2019) 432–444.

[19] A. Frangi, G. Gobat, Reduced order modelling of the non-linear stiffness in mems resonators, International Journal of Non-Linear Mechanics 116 (2019) 211–218.

[20] A. Garg, S. K. Dwivedy, Nonlinear dynamics of parametrically excited piezoelectric energy harvester with 1:3 internal resonance, International Journal of Non-Linear Mechanics 111 (2019) 82–94.

[21] M. Belhaq, Z. Ghouli, M. Hamdi, Energy harvesting in a Mathieu–van der Pol–Duffing MEMS device using time delay, Nonlinear Dynamics 94 (4) (2018) 2537–2546.

[22] R. J. Dolleman, S. Houri, A. Chandrashekar, F. Alijani, H. S. van der Zant, P. G. Steeneken, Opto-thermally excited multimode parametric resonance in graphene membranes, Scientific Reports 8 (1) (2018) 9366.

[23] Y. Huang, J. Fu, A. Liu, Dynamic instability of Euler–Bernoulli nanobeams subject to parametric excitation, Composites Part B: Engineering 164 (2019) 226–234.

[24] P. Alevras, S. Theodossiades, H. Rahnejat, Broadband energy harvesting from parametric vibrations of a class of nonlinear Mathieu systems, Applied Physics Letters 110 (23) (2017) 233901.

[25] M. F. Daqaq, C. Stabler, Y. Qaroush, T. Seuaciuc-Osorio, Investigation of power harvesting via parametric excitations, Journal of Intelligent Material Systems and Structures 20 (5) (2009) 545–557.

[26] Y. Jia, A. A. Seshia, An auto-parametrically excited vibration energy harvester, Sensors and Actuators A: Physical 220 (2014) 69–75.

[27] Y. Jia, J. Yan, K. Soga, A. A. Seshia, Parametric resonance for vibration energy harvesting with design techniques to passively reduce the initiation threshold amplitude, Smart Materials and Structures 23 (6) (2014) 065011.

[28] L. A. Oropeza-Ramos, C. B. Burgner, K. L. Turner, Robust micro-rate sensor actuated by parametric resonance, Sensors and Actuators A: Physical 152 (1) (2009) 80–87.

[29] M. Sharma, E. H. Sarraf, R. Baskaran, E. Cretu, Parametric resonance: Amplification and damping in mems gyroscopes, Sensors and Actuators A: Physical 177 (2012) 79–86.

[30] S. H. Nitzan, V. Zega, M. Li, C. H. Ahn, A. Corigliano, T. W. Kenny, D. A. Horsley, Self-induced parametric amplification arising from nonlinear elastic coupling in a micromechanical resonating disk gyroscope, Scientific reports 5 (2015) 9036.

[31] M. Crespo da Silva, C. Glynn, Nonlinear flexural-flexural-torsional dynamics of inextensional beams. I. Equations of motion, Journal of Structural Mechanics 6 (4) (1978) 437–448.

[32] S. A. M. Lajimi, G. R. Heppler, Free vibration and buckling of cantilever beams under linearly varying axial load carrying an eccentric end rigid body, Transactions of the Canadian Society for Mechanical Engineering 37 (1) (2013) 89–109.

[33] P. M. Osterberg, S. D. Senturia, M-TEST: A test chip for MEMS material property measurement using electrostatically actuated test structures, Journal of Microelectromechanical Systems 6 (2) (1997) 107–118.

[34] S. A. M. Lajimi, Apparatus and method for improved shock, impact, and motion detection, US Patent App. 62/839,378 (May 07 2019).

[35] A. H. Nayfeh, D. T. Mook, Nonlinear oscillations, John Wiley & Sons, 2008.

[36] A. H. Nayfeh, P. F. Pai, Non-linear non-planar parametric responses of an inextensional beam, International Journal of Non-Linear Mechanics 24 (2) (1989) 139–158.

[37] B. Balachandran, A. Nayfeh, Nonlinear motions of beam-mass structure, Nonlinear Dynamics 1 (1) (1990) 39–61.

[38] W. Lacarbonara, A. H. Nayfeh, W. Kreider, Experimental validation of reduction methods for nonlinear vibrations of distributed-parameter systems: analysis of a buckled beam, Nonlinear Dynamics 17 (2) (1998) 95–117.

[39] A. Abusoua, M. F. Daqaq, On using a strong high-frequency excitation for parametric identification of nonlinear systems, Journal of Vibration and Acoustics 139 (5) (2017) 051012.

[40] P. Malatkar, Nonlinear vibrations of cantilever beams and plates, Ph.D. thesis, Virginia Tech (2003).

[41] U. Nabholz, F. Schatz, J. E. Mehner, P. Degenfeld-Schonburg, Spontaneous parametric down-conversion induced by non-degenerate three-wave mixing in a scanning mems micro mirror, Scientific reports 9 (1) (2019) 3997.

[42] A. H. Nayfeh, B. Balachandran, Applied nonlinear dynamics: analytical, computational, and experimental methods, John Wiley & Sons, 2008.

[43] L. D. Zavodney, A. Nayfeh, N. Sanchez, The response of a single-degree-of-freedom system with quadratic and cubic non-linearities to a principal parametric resonance, Journal of Sound and Vibration 129 (3) (1989) 417–442.

[44] A. H. Nayfeh, Nonlinear interactions, Vol. 1, Wiley, New York, 2000.

[45] A. Cowen, G. Hames, D. Monk, S. Wilcenski, B. Hardy, SOIMUMPs design handbook, MEMSCAP Inc.

[46] S. D. Senturia, Microsystem design, Springer Science & Business Media, 2007.

[47] M. Cartmell, J. Roberts, Simultaneous combination resonances in an autoparametrically resonant system, Journal of Sound and Vibration 123 (1) (1988) 81–101.

[48] Selection table for accelerometers | Analog Devices, https://www.analog.com/en/parametricsearch/11175, accessed: 2019-03-20.

[49] D. Elata, H. Bamberger, On the dynamic pull-in of electrostatic actuators with multiple degrees of freedom and multiple voltage sources, Journal of Microelectromechanical systems 15 (1) (2006) 131–140.

[50] W.-M. Zhang, H. Yan, Z.-K. Peng, G. Meng, Electrostatic pull-in instability in mems/nems: A review, Sensors and Actuators A: Physical 214 (2014) 187–218.